AGU ADVANCING EARTH AND SPACE SCIENCES

JGR Solid Earth

RESEARCH ARTICLE
10.1029/2022JB026140

Key Points:

- In situ temperature evolution from an active geyser reveals heat transfer from a bubble trap to the conduit
- Transient measurement reveals the conduit dynamics during the geyser's eruptive cycle
- Details of water jet eruptions captured by high-speed camera

Supporting Information:

Supporting Information may be found in the online version of this article.

Correspondence to:

M. Collignon,
Marine.Collignon@unige.ch

Citation:

Collignon, M., Pioli, L., Trippanera, D., Carrier, A., & Lupi, M. (2023). Conduit processes at the Haukadalur geyser-hosting hydrothermal field (Iceland) revealed by in situ temperature and high-speed camera measurements. *Journal of Geophysical Research: Solid Earth*, *128*, e2022JB026140. https://doi.org/10.1029/2022JB026140

Received 27 NOV 2022
Accepted 16 OCT 2023

Author Contributions:

Conceptualization: Marine Collignon
Data curation: Marine Collignon, Laura Pioli, Daniele Trippanera
Formal analysis: Marine Collignon, Laura Pioli, Daniele Trippanera, Matteo Lupi
Funding acquisition: Matteo Lupi
Investigation: Marine Collignon, Laura Pioli
Methodology: Marine Collignon, Laura Pioli, Daniele Trippanera
Project Administration: Matteo Lupi
Software: Marine Collignon
Supervision: Matteo Lupi
Visualization: Marine Collignon
Writing – original draft: Marine Collignon, Laura Pioli
Writing – review & editing: Laura Pioli, Aurore Carrier, Matteo Lupi

Conduit Processes at the Haukadalur Geyser-Hosting Hydrothermal Field (Iceland) Revealed by In Situ Temperature and High-Speed Camera Measurements

Marine Collignon[1], Laura Pioli[1,2], Daniele Trippanera[3], Aurore Carrier[1,4], and Matteo Lupi[1]

[1]Department of Earth Sciences, University of Geneva, Geneva, Switzerland, [2]Department of Chemical and Geological Sciences, University of Cagliari, Cagliari, Italy, [3]Department of Earth Sciences and Engineering, King Abdullah University of Science and Technology (KAUST), Thuwal, Saudi Arabia, [4]ADRGT, Grenoble, France

Abstract Geysers fascinate scientists and visitors for several centuries. However, many driving mechanisms such as heat transfer in the conduit and in the subsurface remain poorly understood. We document for the first time transient temperature variations inside the active Strokkur's and nearby quasi-dormant Great Geysir's conduits, Iceland. While recording temperature inside the conduit, we visually monitored Strokkur's activity at the vent with a high-speed camera, providing a high temporal resolution of the eruptions. Our results reveal heat transfer from a bubble trap to and through the conduit. We propose a model for the eruptive cycle of Strokkur that includes vapor slug rise, eruption, and conduit refill. Each water jet of an eruption is marked by an initial pulse of liquid water and vapor, emitted at a velocity between 5 and 28 m/s and generally followed by a second pulse less than a second later. The timing of eruptions coincides with temperature maxima in the conduit. After the eruption, the conduit is refilled by water falling back in the pool and drained from neighboring groundwater-saturated geological units. This results in a temperature drop, the amplitude of which increases with depth while its period is reduced. This reflects faster heat transfer in the deeper than shallower part of the conduit. The amplitude of temperature drop following an eruption also increases with the eruption order, implying larger heat release by higher-order eruptions. Temperature in the conduit subsequently increases until the next eruption, starting then a new cycle.

Plain Language Summary Geysers are hot springs that erupt intermittently. Although they have been studied for several centuries, many aspects such as heat transfer in the conduit and subsurface remains poorly understood. We recorded the temperature evolution inside the active Strokkur and quasi-dormant Great Geysir geysers, located 100 m apart, in the Haukadalur hydrothermal field (Iceland). Comparing the timing of eruptions, visually monitored at Strokkur with its temperature records allowed us to characterize the thermal cycle associated with eruptions. Each eruption is marked by a temperature drop and subsequent rise inside the conduit to which we refer as the cooling and warming phases, respectively. We characterize the duration of these phases and the associated temperature variations, which revealed a faster heat transfer in the deeper than shallower part of the conduit and larger heat release by higher-order eruption. A high-speed camera revealed the eruption of a water jet in details. Each jet is marked by a first pulse of liquid water and vapor, emitted at a velocity between 5 and 28 m/s, which is generally followed by a second pulse, less than a second later. We propose a new and complementary model for vapor rise, eruption and, conduit refill of Strokkur.

1. Introduction

Natural geysers are rare geological occurrences. They are hot springs that cyclically discharge steam and liquid water and in minor amounts non-condensable gases (e.g., CO_2) in jetting eruptions (D. White, 1967; Hurwitz et al., 2016). Geysers often occur clustered in hydrothermal fields, like in Yellowstone (USA), Geyser Valley (Russia), and El Tatio (Chile) (Bryan, 1995; Hurwitz & Manga, 2017). Their rarity may be due to the peculiar conditions required for their formation. These are a constant water supply, a heat source converting water into vapor and most importantly a permeable system that allows a stable eruptive cycle (e.g., Ingebritsen & Rojstaczer, 1993, 1996; Kieffer, 1989; Kiryukhin et al., 2012; D. White, 1967). The earliest conceptual models for geyser's plumbing systems were derived mostly from observations of the Great Geysir in Iceland (Bunsen, 1847; Mackenzie, 1811). Temperature measurements in the conduits of various geysers (Droznin et al., 1999; Hutchinson et al., 1997; Munoz-Saez, Manga, et al., 2015; Munoz-Saez, Namiki, & Manga, 2015;

Noguchi et al., 1983; Rinehart, 1969) supported ascent-driven decompression boiling in the conduit as the driving mechanism (Bunsen, 1847). However, further geophysical data and/or direct observations of plumbing systems of eroded geysers revealed the existence of one or several laterally offset cavities connected to the main conduit (Belousov et al., 2013; Cros et al., 2011; Eibl et al., 2021; Vandemeulebrouck et al., 2013, 2014). These observations revive the model initially proposed by Mackenzie (1811), suggesting that eruptions are driven by steam formation in a subsurface cavity. These cavities, known as *bubble traps* act as a reservoir where steam accumulates and periodically discharges into the conduit (Adelstein et al., 2014; Belousov et al., 2013; Mackenzie, 1811; Munoz-Saez, Manga, et al., 2015; Vandemeulebrouck et al., 2013). Although several authors thoroughly investigated the eruptive dynamics using laboratory experiments (Adelstein et al., 2014; Anderson et al., 1978; Namiki et al., 2016; Rudolph & Sohn, 2017; Rudolph et al., 2018) and multi-disciplinary field investigations (Eibl et al., 2021; Munoz-Saez, Manga, et al., 2015; Munoz-Saez, Namiki, & Manga, 2015; Vandemeulebrouck et al., 2014), some aspects of geysering are still poorly understood. While direct exploration provided new insights on the morphology of the main conduit (Belousov et al., 2013; Walter et al., 2020), the general subsurface geometry of these systems are rarely known. Recently, Lupi et al. (2022) investigated the hydrogeological structure of the Haukadalur hydrothermal field, Iceland, and based on geoelectrical surveys have shown the strong control that local tectonics exerts on fluid distribution at depth. Seismic data have been used as a proxy to locate the formation and collapse of the vapor slug, providing basic information on heat transfer in the conduit or in the bubble trap (Eibl et al., 2021; Kedar et al., 1998). However, the role of the bubble trap with respect to the deep aquifer in controlling eruptions remains poorly understood. Our general understanding of heat transfer dynamics and its relevance into conduit processes is still hampered by the limited temperature records of successive eruptive cycles and synchronous temperature measurements of different geysers (e.g., Munoz-Saez, Manga, et al., 2015; Munoz-Saez, Namiki, & Manga, 2015). To fill this gap, we monitored the activity and conduit temperature evolution of the Strokkur and Great Geysir geysers, hosted in the Haukadalur hydrothermal field, Iceland. We selected this hydrothermal field to investigate heat transfer and geyser interaction because of the frequent eruptions and steady recharge at the Strokkur vent (Eibl et al., 2020).

2. The Haukadalur Hydrothermal Field and Its Geysers

The Haukadalur hydrothermal field is located at the eastern margin of the western volcanic rift zone in the Southern lowlands of Iceland (Figure 1) at an altitude of about 100 m a.s.l. The heat fueling hydrothermal circulation is provided by a magmatic system that also fed several eruptions in the Late Pleistocene (Jones et al., 2007; Saemundsson, 1979; Torfason, 1999). The Haukadalur field hosts two famous geysers, Great Geysir and Strokkur, which are amongst the most visited natural touristic attractions of Iceland. This hydrothermal field also hosts hundreds of thermal springs, distributed over a ~3 km^2 area and along NE-SW to N-S directions (Lupi et al., 2022; Pasvanoglu, 1998; Torfason, 1999; Walter et al., 2020). Written documentation of Great Geysir's and Strokkur's activity dates back to 1,294 and 1,789, respectively (Pasvanoglu, 1998). Furthermore tephrochronological studies showed that the hydrothermal field is active for at least 8,000 years (Torfason, 1985). Throughout its known history, Great Geysir's activity has been rejuvenated by large earthquakes before progressively declining and becoming quiescent (Pálmason, 2002; Torfason, 1999). For almost the entire 20th century (1915–2000), the Great Geysir remained inactive unless eruptions were artificially triggered with soap or by lowering the water table (Pálmason, 2002). Two major earthquakes in June 2000 renewed its activity causing the Great Geysir to erupt quasi-yearly. Strokkur's eruptions are different from those of Great Geysir and are characterized by intermittent jets of water into the air with minor amounts of vapor (Torfason, 1999). Strokkur's activity and behavior have also changed through time. From historical records, eruptions between 1789 and 1896 often lasted for more than one hour with longer intervals between eruptions (Pálmason, 2002). Strokkur was inactive for years when in 1963 its eruptions were renewed by drilling the natural conduit from ~23 to 40 m depth (Torfason, 1999). This made eruptions to occur every 8–12 min. Since the earthquakes in 2000, eruptions of Strokkur are two to three time more frequent and fairly constant (Eibl et al., 2020). Based on a 1-year seismic catalog, Eibl et al. (2019) showed that eruptions consist of 1–6 explosion sequences and that the mean repose times ("waiting time") after single to sextuple eruptions before the next eruption linearly increases from 3.7 to 16.4 min. Walter et al. (2020) explored the geometry and average temperature gradient of Great Geysir's and Strokkur's conduits down to 20 m depth. Both conduits in their upper parts (<9–10 m) are pipe-shaped, with a sub-circular section and narrow down from surface to 5 m depth (Figure 3). Below 10 m depth the conduits have an elliptical section. The temperature inside the conduits (measured during quiescent periods) remains below the boiling point of pure water down to 10 m depth (Walter et al., 2020).

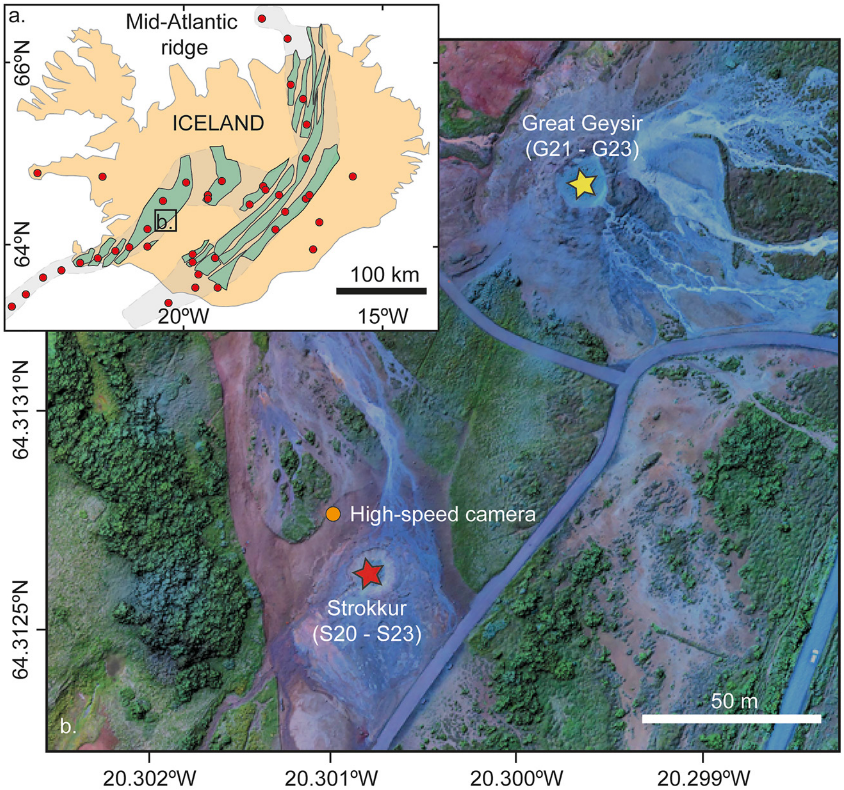

Figure 1. (a) Map of Iceland showing the main volcanoes (red dots) and volcanic systems (green) associated with the mid-Atlantic ridge (light gray) and the geographic position of the field area (black square). (b) Photo of part of the Haukadalur hydrothermal field reconstructed from images acquired with a drone showing the position of Great Geysir (yellow star) and Strokkur (red star). Distance between both geysers is about 110 m. The location of the high-speed (HS) camera used in the field is indicated by the orange dot. During the first night of the recording an infrared (IR) camera was placed next to the HS camera. For the remaining part of the survey, the IR camera was mounted on a drone, which flew over the area. Temperature records S20–S23 and G21–G23 were taken inside the conduits of Strokkur and Great Geysir, respectively.

3. Methods

Between the 20 and 23 June 2018, we recorded the temperature inside both Strokkur's and Great Geysir's conduits at different depths during several hours at night. We immersed two sensors (Hobo U12-015) in the conduits attached to a weighted metallic cable (Table 1, see Supporting Information S1 for further details). In absence of pressure loggers, we estimated the depth of the temperature records from the measured cable length below the water table. We considered a conservative uncertainty of about 1 and 2 m at Strokkur and Great Geysir, respectively. Sensor accuracy ranges from 0.25 to 0.75°C for the recorded temperatures (~60–120°C). The response time of the sensor is not linear but consistent for both sensors and the temperature variations that we tested (Figure 2). The response curve was fitted based on laboratory experiment of water temperature measurements at stabilization times ranging from 1 to 20 min (see Supporting Information S1 for further details). The sensors record 63.2%, 90%, and 99.8% of the temperature variation after 80, 160, and 300 s, respectively. However temperature inversions (i.e., moments where temperature stops increasing and starts decreasing, or vice versa) are instantaneously recorded. Therefore, the timing of temperature minima and maxima inside the geysers is correctly captured but the actual amplitude of the temperature variations is underestimated if the period between minima and maxima is lower than 300 s. Sampling rate was set to 1 Hz.

Date and time of the selected temperature records that are analyzed in this study are reported in Table 1, along with the estimated depth of the sensors. Further in the text, we refer to the temperature records of Strokkur's conduit on the 20 June at 9 and 16 m as 20a and 20b, and on the following nights between 21 and 23 June as S21, S22, and S23, respectively. The temperature records in Great Geyser between 21 and 23 June are referred

10.1029/2022JB026140

Table 1
Characteristics and Basic Statistics of the Temperature Records Measured Inside Great Geysir's and Strokkur's Conduits

					Temperature (°C)				
Recording	Conduit	Depth (m)	Start date	End date	Mean	Std	Min	Max	Median
G21	Geysir	5 ± 2	21/06-00h26′39″	21/06-03h38′19″	75.4	0.62	73.7	77.1	75.4
G22	Geysir	5 ± 2	22/06-00h02′29″	22/06-02h51′59″	66.7	0.98	64.9	68.9	66.7
G23	Geysir	5 ± 2	22/06-21h59′39″	23/06-02h13′19″	74.9	0.73	73	76.7	74.9
S20a	Strokkur	9 ± 1	20/06-01h28′19″	20/06-04h11′39″	100.0	2.35	93.4	106.8	100.5
S20b	Strokkur	16 ± 1	20/06-01h28′19″	20/06-04h11′39″	113.0	3.06	102.7	119.1	113.1
S21	Strokkur	6 ± 1	21/06-00h26′39″	21/06-03h38′19″	90.2	1.46	82.8	94.3	90
S22	Strokkur	10 ± 1	22/06-00h02′29″	22/06-02h51′59″	104.2	2.31	97.7	110.5	104.3
S23	Strokkur	11 ± 1	22/06-21h59′39″	23/06-02h13′19″	106.8	2.88	96.6	112.6	107.1

Note. Depth is given with uncertainty. See method section and Supporting Information S1 for further details.

to as G21, G22, and G23 (Table 1). Analyses and processing of the temperature records were performed with MATLAB 2016a. Temperature raw data, processing scripts and HS videos can be found in Collignon (2022) and Pioli (2023). Before all analyses, the original temperature records were detrended to remove any potential instrumental drift. In addition, they were normalized by their maximum magnitude for spectral analyses to be more easily compared. In parallel with temperature recording, the activity at Strokkur was visually monitored during the recording of S22 and S23 to obtain information on eruption characteristics and timing (using a GPS clock). For S22, we had a visual monitoring between 01h15 and 02h02 only, whereas for S23 the monitoring took place between 22h11 and 23h16 and between 23h37 and 02h14 (GMT).

In this work, we define as an eruption the water jet exiting the pool of the active geyser (i.e., Strokkur). Higher-order eruptions consist of sequences of water jets occurring at interval shorter than 46 s (according to the observation of Eibl et al. (2021)). The order of an eruption (e.g., double, triple, …) is given by the number of water jets in the sequence. Within a continuous water jet, we distinguish pulses (rapid increases in exit speed associated to flow bursts), which are spaced by a few seconds or less, and occur within a continuous jet.

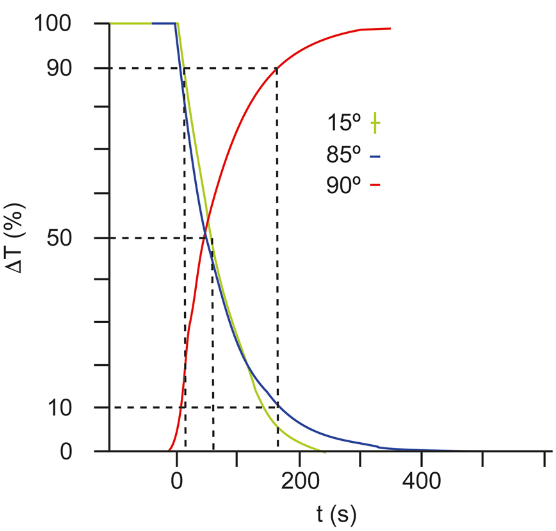

Figure 2. Response curve of the Hobo sensor to instantaneous temperature variations. The response curve is normalized to the temperature difference. The width and height of lateral and vertical bars (to the right) represent measurement errors of the same color curve and numbers are the absolute temperature variation (see text for more details).

Fourteen eruptions were recorded by HS videos at a resolution of 700 fps and 512 × 800 pixels. The Phantom MIRO camera was connected to an AF Micro-Nikkor 35 mm f/2.8D lens at a distance of about 10 m from Strokkur's vent. Further details can be found in Supporting Information S1. Movies were analyzed using the FIJI software (Schindelin et al., 2012) to measure the eruption timing and vertical exit speeds. The eruption duration was calculated as the time between onset and end of emission of the steam and water jet. Duration estimations have uncertainties of 1/fps = 1.4 ms. Images, extracted from the videos, were calibrated based on the internal vent diameter of Strokkur as seen along the image plane and confirmed by drone images depicting the recording station. The vent diameter was measured based on a georeferenced orthomosaic of the area (Figure 1), obtained from optical images acquired with a 20 Mpx camera mounted on a quadcopter (Phantom 4 Pro). 417 high-resolution aerial photographs, with 75% of both front and side overlap, were acquired by the drone, while flying at 65 m of altitude. An orthomosaic and a Digital Surface Model, with a resolution of 1.6 and 3.2 cm/px, respectively were obtained after the Structure from Motion processing, performed with Agisoft Metashape©. We reduced the reconstruction error below 3 cm/px by placing 10 markers in the field and measuring them with a kinematic GPS.

Journal of Geophysical Research: Solid Earth 10.1029/2022JB026140

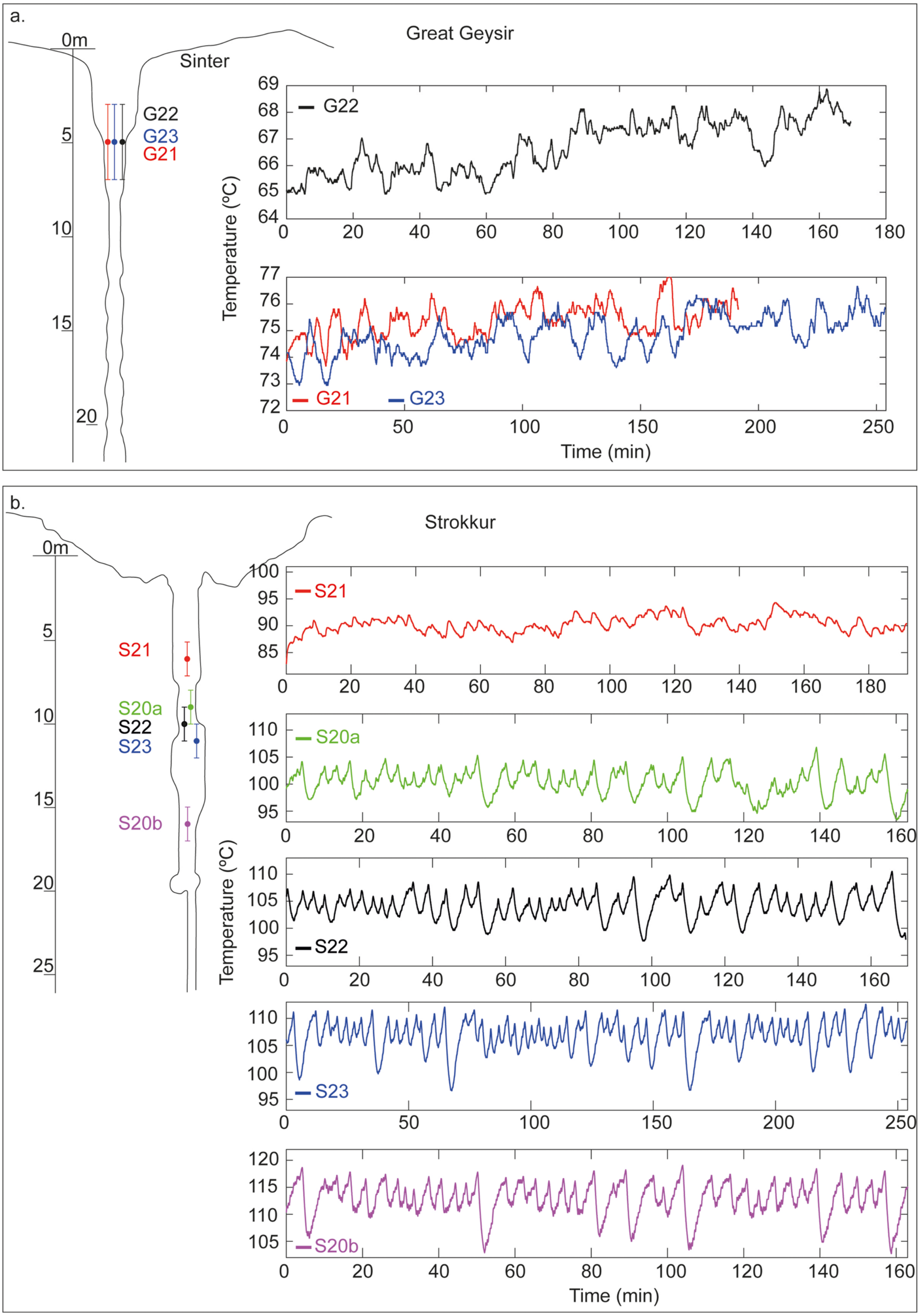

Figure 3. Schematic representation of the conduits with the temperature records inside (a) Great Geysir and (b) Strokkur during the nights 20–23 June 2018. The records depth and associated uncertainty are represented inside the conduits (left) by a dot and error bar, respectively, using the same color code than the data (right). Records are sorted by depth. The conduit shapes are taken from Eibl et al. (2021) and Torfason (1985) (reported also in Pasvanoglu (1998)) for Strokkur and Great Geysir, respectively.

Table 2
Statistics of the Thermal Cycles for Great Geysir Records

Name	Variable	Units	Mean	Std	Min	Max	Median	Pts
G21	ΔT_c	°C	1.08	0.49	0.51	2.17	0.88	22
	Δt_c	sec	306	183	70	873	282	22
	$\Delta T_c/\Delta t_c$	°C/min	0.26	0.13	0.08	0.56	0.23	22
	ΔT_w	°C	1.11	0.52	0.44	2.30	0.92	22
	Δt_w	sec	193	134	46	467	158	22
	$\Delta T_w/\Delta t_w$	°C/min	0.48	0.28	0.12	1.22	0.44	22
	T_b	sec	499	266	131	1,224	411	22
G22	ΔT_c	°C	0.98	0.48	0.40	2.30	0.92	27
	Δt_c	sec	208	136	21	549	177	27
	$\Delta T_c/\Delta t_c$	°C/min	0.38	0.24	0.06	1.25	0.33	27
	ΔT_w	°C	0.99	0.52	0.35	2.18	0.95	27
	Δt_w	sec	149	123	22	439	108	27
	$\Delta T_w/\Delta t_w$	°C/min	0.59	0.35	0.15	1.43	0.52	27
	T_b	sec	358	206	83	831	297	27
G23	ΔT_c	°C	1.12	0.57	0.46	2.52	0.97	28
	Δt_c	sec	274	151	87	574	223	28
	$\Delta T_c/\Delta t_c$	°C/min	0.26	0.09	0.15	0.55	0.25	28
	ΔT_w	°C	1.1	0.53	0.47	2.29	0.99	28
	Δt_w	sec	232	181	40	758	188	28
	$\Delta T_w/\Delta t_w$	°C/min	0.43	0.27	0.08	1.26	0.34	28
	T_b	sec	505	281	146	1,141	458	28

Note. T_b: Period of the thermal cycle (i.e., time interval between two maxima). ΔT_c: temperature variation during the cooling phase. Δt_c: period of the cooling phase. ΔT_w: temperature variation during the warming phase. Δt_w: period of the warming phase. $\Delta T_c/\Delta t_c$ and $\Delta T_w/\Delta t_w$ are the temperature variations during the period of the cooling and warming phases, respectively and are reported here as an indication. Min: minimum, max: maximum, std: standard deviation, and pts: number of thermal cycles.

4. Results

4.1. Temperature Records at Great Geysir and Strokkur

Temperature records at Great Geysir were obtained at a similar depth of 5 ± 2 m. However, while G21 and G23 display comparable average temperatures (75.4 and 74.9°C, respectively), G22 presents an average temperature about 8°C lower (Figure 3a, Table 1). Water temperature in Strokkur's conduit is higher than at Great Geysir and also positively correlated with the estimated depth (Table 1, Figure 3b). It is on average 90.2, 100, 104, 107, and 113°C at 6, 9, 10, 11, and 16 m, respectively.

Despite the quiescence of Great Geysir, all temperature records show clear oscillations (Figure 3). However, their amplitude, period, and shape vary between both geysers. We describe and analyze these oscillations based on the identification of the most prominent peaks (i.e., minima and maxima, see Supporting Information S1 for further details). We define a thermal cycle as the oscillation between two temperature maxima. Each cycle comprises a cooling phase, between the maximum and minimum, and a warming phase between the minimum and maximum. For each phase, we analyze the amplitude (i.e., ΔT) and period (i.e., Δt), as well as the period (i.e., T_b) of thermal cycles (Tables 2 and 3).

G21, G22, and G23 displays similar oscillations of about 1°C that may be separated by a few minutes of steady conditions, with temperature variations in the range of the instrument resolution. These periods of steady conditions can be seen for example, between 95 and 102 min on G22 or between 188 and 202 min on G23 (Figure 3a). For all records, the cooling phase lasts longer than the warming phase. In details, however, the oscillations of G22 are slightly different from those of G21 and G23, which present similar characteristics (Table 2). The period of a thermal cycle is on average 358 s for G22, against ca. 500 sec for G21 and G23. The amplitude of the oscillation is slightly lower for G22, with on average 1°C, against 1.1°C for G21 and G23.

Temperature oscillations recorded at Strokkur are generally more regular than those of Great Geysir records, with higher amplitudes (up to 15°C) that also increase with depth (Figure 3b, Table 1). The relative duration of the cooling and warming phases of the thermal cycles changes with depth, varying the shape of the oscillations of Strokkur records (Figure 3b). The shallowest record, S21, shows cooling phases that are on average 90 s longer than the warming phases (Table 3). S21 oscillations have a lower amplitude (~2.3°C) than for the other records of Strokkur (>4°C) and are sometimes interrupted by short periods (2–3 min) of steady conditions, with temperature variations within the instrument resolution, as observed for Great Geysir. The deepest record, S20b, displays warming phases that are on average 120 s longer than the cooling phases (Table 3). The warming phases of temperature records around 10 m depth (S20a, S22, and S23) are slightly longer (less than 1 min) than their cooling phases, so that the oscillations look less asymmetrical than those of S20b and S21. The period of a thermal cycle is on average similar between Strokkur records (about 250 s), with the exception of S21, which has a longer period of 360 s (Table 3).

The spectrograms of the temperature records highlight the main frequencies through time. A frequency peak becomes dominant when its power/frequency intensifies. All spectrograms of Great Geysir highlight a main frequency peak around 1 mHz (Figure 4a). A second frequency peak around 0.5 mHz is visible for G21 and G23, and around 0.25 mHz for G22. Frequencies of 0.25, 0.5, and 1 mHz have corresponding periods of 1,000, 2,000, and 4,000 s, respectively, which are not consistent with the average duration of the thermal cycles (360 and 500 s). Instead they reflect significant changes in the periodicity of the signal during the recording time. Spectrograms of the synchronous S21, S22, and S23 records show distinct patterns (Figure 4b). They all present a broad frequency peak between 1 and 2 mHz, the power/frequency of which varies during the recording time. It intensifies between 84 and 120 min for S22, as well as between 60 and 90 min and between 150 and 180 min

Table 3
Statistics of the Thermal Cycles for Strokkur Records

Name	Variable	Units	Mean	Std	Min	Max	Median	Pts
S21	ΔT_c	°C	2.34	1.02	1.01	5.31	2.20	30
	Δt_c	sec	224	84	114	404	206	30
	$\Delta T_c/\Delta t_c$	°C/min	0.64	0.21	0.25	1.09	0.61	30
	ΔT_w	°C	2.27	1.08	1.00	5.00	1.93	30
	Δt_w	sec	135	114	22	439	95	30
	$\Delta T_w/\Delta t_w$	°C/min	1.53	0.92	0.46	3.72	1.37	30
	T_b	sec	359	161	136	794	328	30
S20a	ΔT_c	°C	4.61	2.43	1.40	11.40	4.32	37
	Δt_c	sec	100	40	30	229	91	37
	$\Delta T_c/\Delta t_c$	°C/min	2.78	0.83	1.26	4.53	2.63	37
	ΔT_w	°C	4.69	1.95	1.86	9.99	4.30	37
	Δt_w	sec	148	68	28	310	134	37
	$\Delta T_w/\Delta t_w$	°C/min	2.08	0.74	1.11	5.07	1.95	37
	T_b	sec	248	81	118	452	231	37
S22	ΔT_c	°C	5.18	2.21	2.19	11.84	4.44	39
	Δt_c	sec	114	24	79	180	108	39
	$\Delta T_c/\Delta t_c$	°C/min	2.64	0.64	1.40	3.99	2.57	39
	ΔT_w	°C	5.25	1.99	2.29	12.15	4.91	39
	Δt_w	sec	140	71	48	413	122	39
	$\Delta T_w/\Delta t_w$	°C/min	2.38	0.45	1.62	3.62	2.38	39
	T_b	sec	254	89	130	593	241	39
S23	ΔT_c	°C	5.87	2.99	1.94	15.46	4.95	58
	Δt_c	sec	102	28	49	188	96	58
	$\Delta T_c/\Delta t_c$	°C/min	3.32	0.82	1.51	5.19	3.29	58
	ΔT_w	°C	5.84	3.02	1.92	14.61	4.72	58
	Δt_w	sec	154	88	28	458	127	58
	$\Delta T_w/\Delta t_w$	°C/min	2.42	0.60	1.37	4.46	2.33	58
	T_b	sec	256	112	109	646	215	58
S20b	ΔT_c	°C	6.95	3.26	2.64	15.62	6.07	37
	Δt_c	sec	69	19	38	110	67	37
	$\Delta T_c/\Delta t_c$	°C/min	6.03	1.94	3.18	10.23	5.72	37
	ΔT_w	°C	6.96	2.74	3.32	13.93	6.26	37
	Δt_w	sec	179	74	79	359	163	37
	$\Delta T_w/\Delta t_w$	°C/min	2.40	0.46	1.42	3.52	2.47	37
	T_b	sec	248	83	117	456	232	37

Note. T_b: Period of the thermal cycle (i.e., time interval between two maxima). ΔT_c: temperature variation during the cooling phase. Δt_c: period of the cooling phase. ΔT_w: temperature variation during the warming phase. Δt_w: period of the warming phase. $\Delta T_c/\Delta t_c$ and $\Delta T_w/\Delta t_w$ are the temperature variations during the period of the cooling and warming phases, respectively and are reported here as an indication. Min: minimum, max: maximum, std: standard deviation, and pts: number of thermal cycles. Table entries are sorted by depth (see Figure 3).

for S23. The temperature records during these periods show larger amplitude and longer periodicity oscillations (Figure 4b). Another less dominant frequency peak around 4 mHz is visible on the S22 and S23 spectrograms (Figure 4b). Its corresponding period of 4.2 min is consistent with the duration of the thermal cycles at Strokkur (Table 3).

4.2. Strokkur's Eruption and Temperature Variation

To compare the geysering activity with the temperature records, we visually monitored the eruptions at Strokkur during the nights of 22 and 23 June and recorded the timing (with a gps calibrated clock) of 78 jets, as well as the time interval between them. Based on previous work (Eibl et al., 2020), jets erupting within less than 46 s are expected to belong to the same eruption of higher-order (double, triple, etc). We thus witnessed 49 single, 10 double, and 3 triple eruptions (gray areas in Figures 5a and 5b). We did not observe higher-order (i.e., 4, 5 or 6) eruptions as reported by Eibl et al. (2020). We note a correlation between the eruptions and maxima of synchronous temperature records (Figures 5a and 5b). All observed eruptions coincide, within a timing uncertainty of a few seconds, with most temperature maxima associated with an eruption (Figures 5c and 5d). Only two small temperature peaks around 23h39 and 01h44 (black triangle in Figure 5b) during our monitoring could not be linked to a visible eruption at the surface. However, we also occasionally observed a bulge of the water table. The water table returned to its original level and was not followed by a water jet as this would typically happen during an eruption. This phenomenon was previously described at Strokkur and referred to as *aborted eruption* (Eibl et al., 2020; Walter et al., 2020). The temperature maxima of double and triple eruptions are reached just before the last water jet (Figures 5c and 5d). An eruptive cycle corresponds thus to a thermal cycle and its duration is the time interval after eruption (time after eruption [TAE]) of Eibl et al. (2020). Based on our direct observations, we distinguish between thermal cycles following eruptions of different orders (Figure 6). We characterize the temperature evolution at 10 m depth within Strokkur's conduit during the cooling and warming phases of the eruptive cycles, as S22 and S23 were recorded at the same depth given the uncertainty. Further statistics for this analysis are reported in Supporting Information S1.

The duration of the thermal cycles increases with the eruption order (Figure 6a). We observe that the recorded temperature variations for both the cooling and warming phases increase with the eruption order from ∼4.5°C for single to ∼13.5°C for triple eruptions (Figure 6b). The temperature profiles show a distinct negative incursion after double and triple eruptions that is more pronounced than for single eruptions (Figure 5). For the considered triple eruptions, the temperature variation is on average larger for the cooling than the warming phase. The duration of both cooling and warming phases after the eruption increases with the eruption order; but this increase is larger for the warming than the cooling phase (Figure 6c). The cooling phase lasts on average 1.6 ± 0.8, 2.4 ± 0.3, and 2.8 ± 0.4 min for single, double, and triple eruptions, respectively. The warming phase lasts on average 2.1 ± 0.8, 4.4 ± 1.4, and 5.8 ± 1.8 min for single, double, and triple eruptions, respectively. However, the actual temperature variations need to be calibrated based on the sensors' response curves. Considering an almost instantaneous temperature drop associated with the eruption discharge and the recorded duration of the cooling phases, we estimate that the sensors recorded about 70%, 85%, and 90% of the temperature drop for single, double, and triple

10.1029/2022JB026140

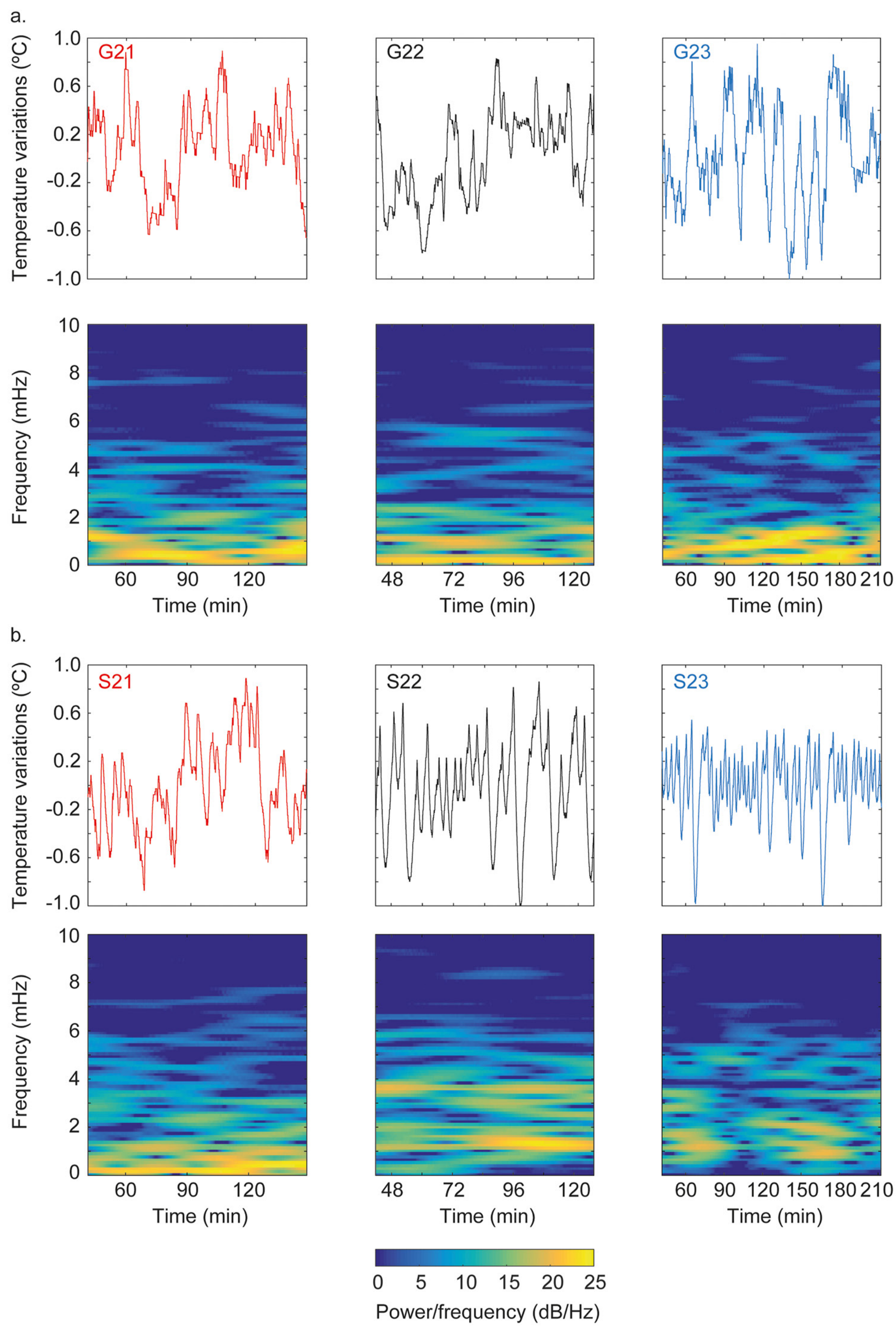

Figure 4. Normalized signals and associated spectrograms of temperature recorded inside (a) Great Geysir and (b) Strokkur. Color codes of temperature signals are the same as in Figure 3.

eruptions during the cooling phase, respectively. The estimated temperature drop experienced inside Strokkur at ~10 m depth would thus be about 6.2, 11.5, and 15.5°C for single, double, and triple eruptions, respectively. The more complex pattern of temperature rises recorded by the sensors (Figure 5) could hardly be explained by an instantaneous temperature rise. Therefore, a calculation of the real temperature variation during the warming phase would not be accurate.

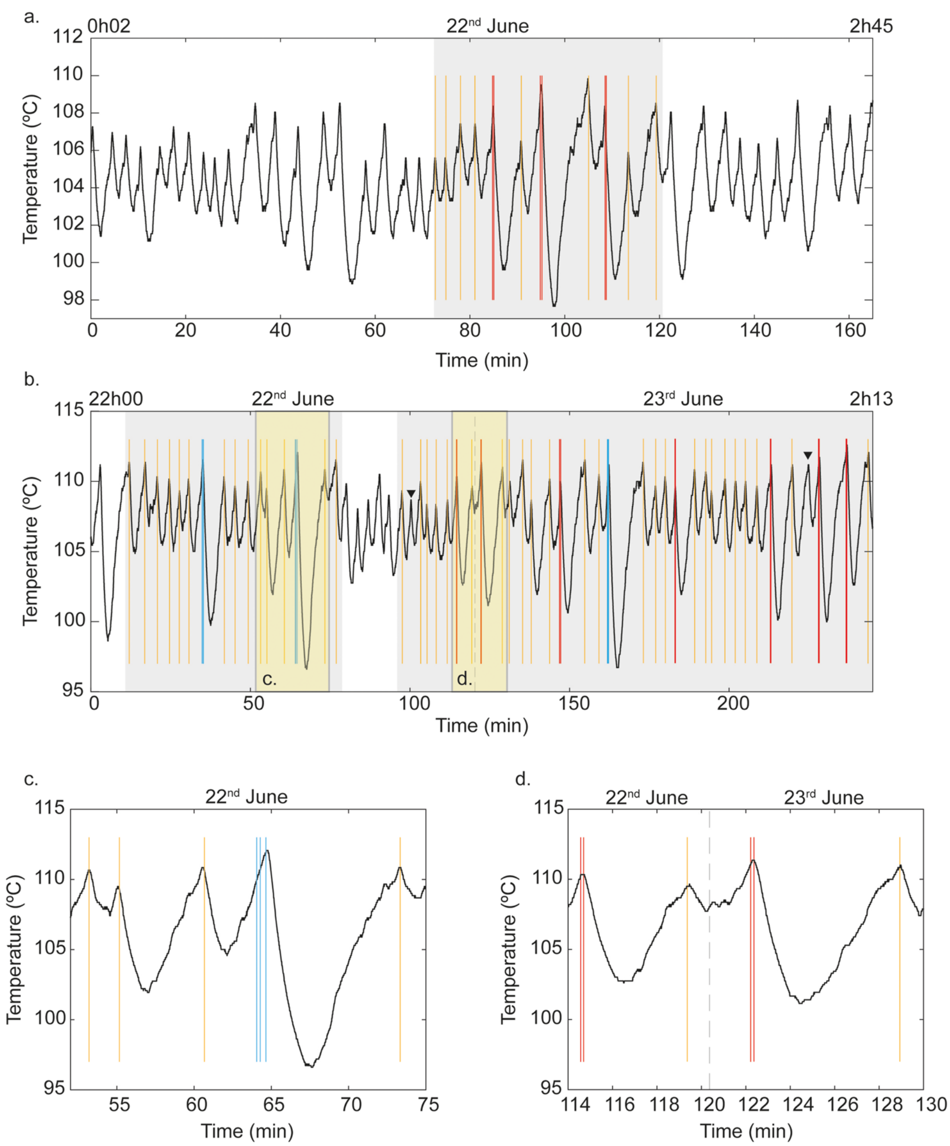

Figure 5. Temperature variation and eruptions at Strokkur. (a) S22 and (b) S23 records. (c, d) Zooms in S23 record. Orange vertical lines: single eruptions. Red vertical lines: jets of double eruptions. Blue vertical lines: jets of triple eruption. Black triangle: aborted eruptions. Gray areas: period of visual monitoring of Strokkur's activity. Yellow area: selected data shown in panels (c, d).

4.3. Temperature Variation Within the Conduit During the Eruptions

All records excepting S21 show clear oscillations that can be used as proxy for eruption identification. A few selected peaks could correspond to aborted eruptions, but based on our monitoring, we assume that their number is statistically irrelevant. We analyze the synchronous S20a and S20b records to provide a direct comparison of the temperature evolution during eruptive cycles at different depths (Figure 7). Eruption cycles were obtained from an automatic peak selection. We also manually correct eventual missing/inserted peaks after visual inspection to obtain the same number (and synchronous) eruptions between S20a and S20b. We identified 31 single and 6 double eruptions (Table 4). We could not identify any triple eruption. Further details about peak selection can be found in Supporting Information S1.

The amplitude of temperature oscillation increases with both depth and eruption order (single or double, Figure 7). The warming phase of the deepest record, S20b, is also marked by high-frequency and minor amplitude oscillations, which are less pronounced for S20a. Temperature maxima of S20a and S20b, marking the timing of eruptions, coincide within a few seconds. This reflect the sudden emptying of the conduit, at least a large part of

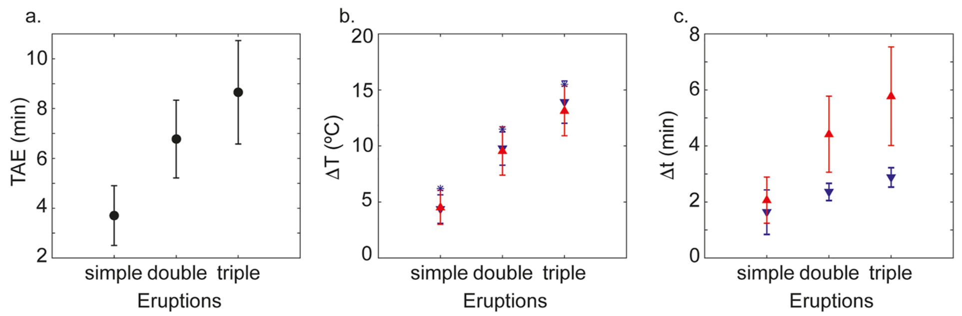

Figure 6. Analysis of observed eruptions. (a) Time after eruption of observed single, double, and triple eruptions. (b) Temperature variation (ΔT) and (c) associated period (Δt) for the warming (red) and cooling (blue) phases of eruptive cycles and for single, double, and triple eruptions. Mean value (triangle or circle) and standard deviation (error bars) are reported in the graphs for the recorded temperature and time. The real temperature drops, estimated from the response time curves are shown in panel (b) by the blue asterisks. Statistics of the analysis are presented in Table S4 in Supporting Information S1.

it, during the eruption. The minima, however, are not synchronous. S20a minima may occur up to 90 s after those of S20b (Figure 7b), reflecting a delay in the heating up of conduit between its lower and upper parts after an eruption.

The magnitude of temperature variations increases with depth for both the cooling and warming phases, regardless of the eruption order (Figures 8a and 8c). For single eruptions, the recorded temperature variations are similar between the cooling and warming phases, with on average an amplitude of 3.8 and 5.6°C at 9 and 16 m depth, respectively (Figure 8a, Table 4). For double eruptions, the magnitude of recorded temperature variations is on average slightly higher in the cooling than warming phases but it is generally around 8.5°C at 9 m depth and around 13°C at 16 m depth for both phases (Figure 8c, Table 4). As previously, the true temperature drop for the cooling phase can be evaluated based on its duration and the sensors' response curve. The average temperature

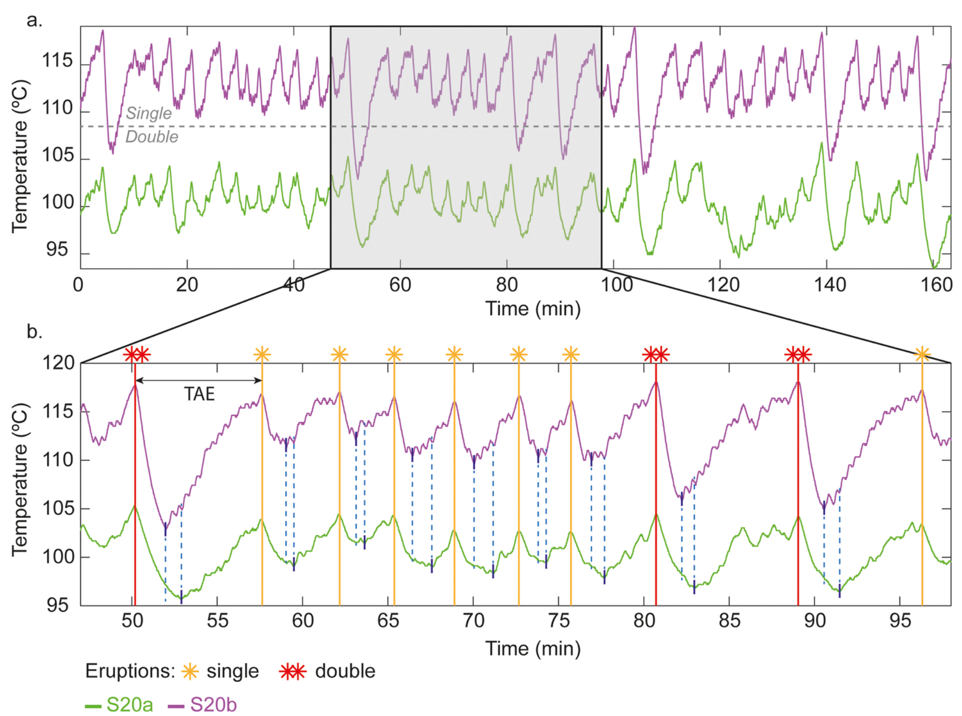

Figure 7. (a) Temperature recorded during the 20 June 2018 at 9 m (S20a, green line) and 16 m (20b, purple line). (b) Closer view on temperature signals between 45 and 100 min. Single and double eruptions are marked by orange and red asterisks, respectively. The timing of maxima (i.e., eruption) and minima is projected on each signal with the vertical bars. Respectively, orange and red for maxima and dashed blue lines for minima. The time after eruption is shown by the black double arrows.

Table 4
Statistics of Eruptive Cycles Observed During the 20 June 2018 at Two Different Depths (S20a: 9 ± 1 and S20b: 16 ± 1)

Record and eruption type	Variable	Units	Mean	Std	Min	Max	Median	Pts
20a single	ΔT_c	°C	3.79	1.50	1.40	7.08	3.54	31
	Δt_c	sec	93	40	30	229	84	31
	$\Delta T_c/\Delta t_c$	°C/min	2.56	0.69	1.26	4.42	2.51	31
	ΔT_w	°C	4.08	1.32	1.86	6.66	4.24	31
	Δt_w	sec	127	48	28	212	127	31
	$\Delta T_w/\Delta t_w$	°C/min	2.12	0.79	1.11	5.07	2.02	31
	TAE	sec	220	48	118	312	216	31
20b single	ΔT_c	°C	5.63	1.22	2.64	7.47	5.65	31
	Δt_c	sec	64	15	38	99	62	31
	$\Delta T_c/\Delta t_c$	°C/min	5.52	1.65	3.18	10.23	5.47	31
	ΔT_w	°C	5.93	1.37	3.32	9.59	5.86	31
	Δt_w	sec	155	48	79	258	151	31
	$\Delta T_w/\Delta t_w$	°C/min	2.39	0.49	1.42	3.52	2.44	31
	TAE	sec	219	48	117	313	210	31
20a double	ΔT_c	°C	8.88	1.73	6.93	11.40	8.62	6
	Δt_c	sec	136	21	99	159	138	6
	$\Delta T_c/\Delta t_c$	°C/min	3.92	0.46	3.41	4.53	3.91	6
	ΔT_w	°C	7.87	1.60	6.15	9.99	7.67	6
	Δt_w	sec	257	46	176	310	261	6
	$\Delta T_w/\Delta t_w$	°C/min	1.86	0.32	1.43	2.28	1.82	6
	TAE	sec	393	55	307	452	398	6
20b double	ΔT_c	°C	13.74	1.29	12.11	15.62	13.38	6
	Δt_c	sec	96	11	85	110	93	6
	$\Delta T_c/\Delta t_c$	°C/min	8.66	0.91	7.11	9.66	8.83	6
	ΔT_w	°C	12.27	1.58	9.92	13.93	12.49	6
	Δt_w	sec	303	59	218	359	322	6
	$\Delta T_w/\Delta t_w$	°C/min	2.47	0.24	2.09	2.73	2.49	6
	TAE	sec	399	60	303	456	416	6

Note. ΔT_c, Δt_c, and $\Delta T_c/\Delta t_c$ are respectively the magnitude of the temperature variation, the associated time and temperature rate of the cooling phase of the eruptive cycle. ΔT_w, Δt_w, and $\Delta T_w/\Delta t_w$ are respectively the magnitude of the temperature variation, the associated time and temperature variation over time of the warming phase of the eruptive cycle. TAE: time after eruption, min: minimum, max: maximum, std: standard deviation, and pts: number of eruptive cycles. Table entries are sorted by eruption order and depth (see Figure 3).

drop after single eruption is estimated at 5.4 and 10.2°C at 9 and 16 m, respectively (Figure 8a). For double eruptions, it is about 10.4 and 19.6°C at 9 and 16 m, respectively (Figure 8c). Duration of the cooling phase decreases with depth, whereas the warming phase is longer at deeper depths (Figures 8b and 8d). The cooling phase lasts on average 1.6 ± 0.7 min at 9 m depth and 1.1 ± 0.3 min at 16 m depth for single eruptions, whereas for double eruptions it drops from 2.3 ± 0.4 min at 9 m depth to 1.6 ± 0.2 min at 16 m depth. The warming phase lasts on average 2.1 ± 0.8 min at 9 m depth and 2.6 ± 0.8 min at 16 m depth for single eruptions, whereas for double eruptions it increases from 4.3 ± 0.8 min at 9 m depth to 5 ± 1 min at 16 m depth (Figures 8b and 8d).

4.4. Single Eruption Dynamics

Further information on eruption dynamics was obtained from HS recordings of the single explosions listed in Table S1 in Supporting Information S1, whose duration ranges from 1.5 to >3 s (minimum duration of eruption

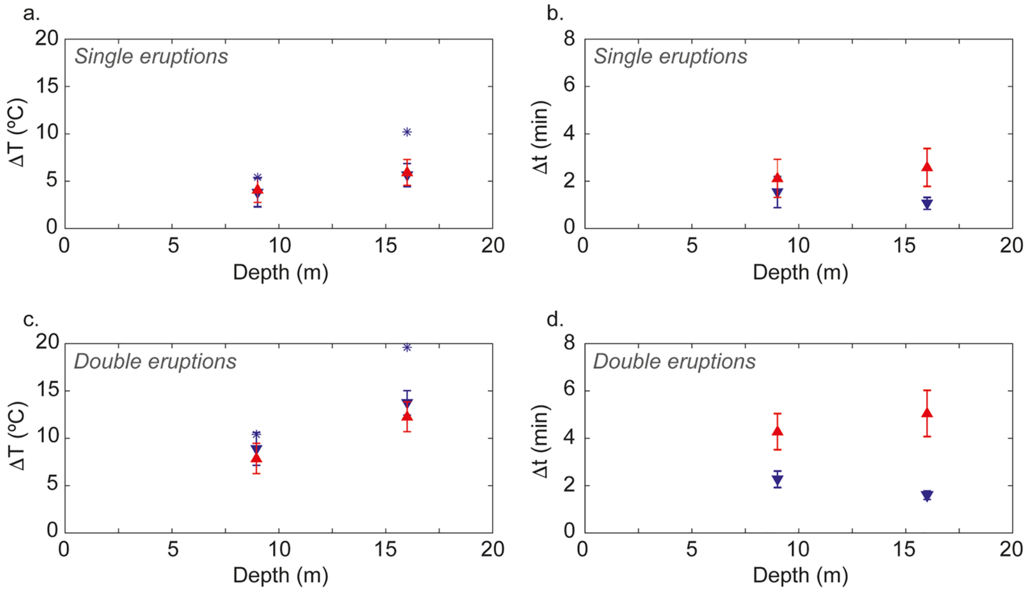

Figure 8. Analysis of eruptions. Temperature variation (ΔT) and associated period (Δt) for the warming (red) and cooling (blue) phases of (a, b) single and (c, d) double eruptions at different depths. Mean value (triangle) and standard deviation (error bars) for the recorded temperature and timing are reported in the graphs. The real temperature drops, estimated from the response time curves are shown in (a, c) by the blue asterisks. Selected minina and maxima for the analysis are presented in Figure S6 in Supporting Information S1. Statistics are reported in Table 4.

not fully captured by the recordings, Table S1 in Supporting Information S1). These eruptions were always anticipated by a bulging of the water free surface atop the vent, and rapidly followed by the rise of a turbulent vapor pocket which eventually broke the liquid film and started a vertical jet of mixed vapor and water droplets. The free liquid surface rose above the vent at speeds generally <1 m/s, while the speed of bubble rise, as it emerged above the vent and reached the top of the bulge, ranged from 1 to 4 m/s. The initial pulse was followed in most jets by a faster second pulse at 0.7 ± 0.3 s after the first one. About half of the eruptions ended with the second pulse, while the remaining ones were marked by a third, low-energy pulse following the second one after 0.5 ± 0.5 s (Figure 9). Finally, one eruption showed a fourth pulse, occurring at 0.9 s after the third one (Figure 9). The initial pulse was ejected at exit speeds ranging from 5 to 28 m/s. Measured speeds of the jet associated with the second pulse range from 4 to 30 m/s. The jet associated with final and third pulses are generally <10 m/s. Water from the jet fell almost completely back into the conduit pool, except for the fine spray which was dispersed in the atmosphere. Because of their typically larger ejection speed and similar duration with respect to the other pulses, we assume that most of the mass is released during the second pulses. Few eruptions have shown that bulging before eruption was clearly associated with the rise of multiple bubbles each occupying a portion of the conduit. Thermal videos recorded water jet temperatures at the vent of 68–72°C. This agrees well with the most superficial temperatures measured in the conduit. No significant temperature difference was noted among pulses within the same eruption.

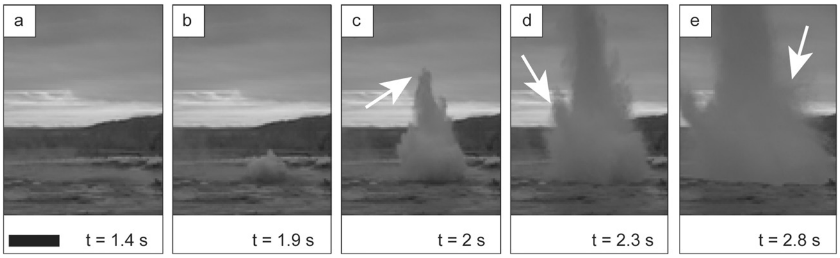

Figure 9. Type dynamics of eruption jet at Strokkur. Scale bar is 3 m long. (a) Initial bulging, (b) break up of the free surface, (c) initial jet formed by multiple spikes, (d) second pulse while the first jet is already collapsing, and (e) third small pulse covered by fallout of previously ejected water.

10.1029/2022JB026140

5. Discussion

5.1. Comparison With Previous Temperature Data

Our temperature data represent the first continuous recordings of several hours inside the conduits of Great Geysir and Strokkur. They can thus reveal the thermal conditions inside the conduits during the eruptive behavior of the geysers (at least for Strokkur), which were until now unknown. Previous studies have punctually measured the temperature inside the conduits between eruptions, leading to steady temperature profiles for both Great Geysir and Strokkur (Pasvanoglu, 1998; Torfason, 1985; Walter et al., 2020). Eibl et al. (2021) continuously recorded the temperature in the pool and outflow channel of Strokkur during its eruptive activity but not inside the conduit.

Recorded temperatures at Great Geysir vary between 64.9 and 77.1°C, with large discrepancies between the recording nights. G21 and G23 show a comparable average temperature of ∼75°C, against 66.7°C for G22. The large difference could be related to the uncertainty in the recording depths (±2 m), which would imply a steep thermal gradient in the upper part of the conduit. Yet, Walter et al. (2020) measured a steady temperature of ∼90°C from the surface down to 10 m below water at Great Geysir. Torfason (1985) measured a steady temperature of ∼80°C in the first 7 m, followed at depth by a progressive increase. We instead associate the temperature decrease of G22 to temporary cooling of the shallow system associated with rain that occurred during the recording. According to the weather records, at the Hjarðarland station (Supporting Information S1), between 1 and 1.5 mm of rain fell during a period of 12 hr around the recording of G22. The sensor was likely placed in the portion of the conduit just before it narrows down and we recorded the temperature variation at the pool/conduit limit, where water temperature can strongly be affected by surface conditions (e.g., weather). Our measured temperatures are in the lower range of previously recorded temperatures for Great Geysir: up to 90°C at one meter water depth in 2016 and down to 73°C at the surface in 1998 (Pasvanoglu, 1998; Walter et al., 2020).

Temperature at the surface of Strokkur is similar to the previous records of 2016–2018 (Eibl et al., 2020; Walter et al., 2020). None of the weather data collected at the nearby stations show a correlation with the water temperature at Strokkur (see Supporting Information S1), confirming that the variations observed between the different nights reflect changes in the sensor depth. Considering the thermal gradient measured by Walter et al. (2020), our depth estimates are consistent with the corresponding recorded temperatures (average), within the uncertainty range (i.e., 1 m). Eibl et al. (2021) reported the temperature evolution in the pool and outflow channel of Strokkur during an eruptive cycle. Their temperature records show low amplitude variations with a broad but weak thermal peak after the eruption. This peak is delayed in time in the outflow channel record because it was taken further away from the conduit than the pool record. Identification of the eruptive phases described by Eibl et al. (2021) is, however, not possible from their temperature records because of the too low amplitude of the oscillations.

5.2. Identification of Strokkur's Eruptions

By convention an eruptive cycle starts with the onset of an eruption (Kieffer, 1984). In our study we use the temperature data as a proxy to identify eruptive cycles of Strokkur, assuming that the temperature maxima coincide with the eruptions. This assumption is less accurate for higher-order eruptions, because the temperature peak does not coincide with the first but the last water jet of a sequence. The time interval between the water jets is 13.9 ± 4.8 s for double eruptions and 13.5 ± 4.6 s for triple eruptions, based on our monitoring. These values are slightly lower than the 15.6 ± 4.5 and 17.9 ± 5.5 s, reported by Eibl et al. (2020) for double and triple eruptions, respectively, on a much larger data set. The duration of the warming phase of the previous eruptive cycle will be overestimated by ca. 10–20 s. The amplitude of temperature variation during this time interval will also be overestimated, by up to 0.5° (Figure 3). Further deviations could also occur when estimating the phase duration from automatic selection of minima and maxima if a temperature plateau is present. They are usually present around both minima and maxima and last between 5 and 10 s. As a result, there is an uncertainty of a few seconds to the estimation of the duration of the eruption phases.

We could not capture the true temperature pattern during an eruptive cycle because of the response time of the sensors (Figure 2). Yet, temperature inversions were accurately captured, allowing reliable quantification of the duration of the cooling and warming phases. We assumed an instantaneous temperature drop after the eruption to estimate its actual value from the response time curve. This assumption implies that most of the energy will be released during the eruption. In any case, the temperature variations are significantly different between the eruption types (at least 4–5°C after correction) or the recording depth to reflect a variability inside Strokkur's conduit and not a recording bias. We observe that the temperature variations increase with depth and the eruption order in a similar manner for both the warming and cooling phases. However, the phase duration increases with the eruption order significantly more for the warming than cooling phases. Moreover, the phase duration slightly increases with depth for the warming phase while it decreases for the cooling phase, changing the symmetry of the oscillations between the different signals (Figure 3).

We identified and analyzed the oscillations for 107 single, 21 double, and 4 triple eruptions from the S20a, S22, and S23 records. Unless two higher-order eruptions follow each other (it only happened once), the period between two temperature maxima corresponds to the TAE defined by Eibl et al. (2020). We observed TAEs of 3.7 ± 1, 6.5 ± 1.2, and 8.8 ± 1.7 min for single, double, and triple eruptions, respectively. These values are in good agreement with previous TAEs measured by Eibl et al. (2020) and attest of the regularity of Strokkur's eruptions. The analysis on the temperature oscillations yields similar results to the one shown in Figure 6. The mean values remain almost the same but the standard deviations are reduced for both single and double eruptions due to a larger data set (see Figures S7, S8 and Table S6 in Supporting Information S1). In absence of synchronous seismic data or camera monitoring the water surface, the identification of the eruption type from the temperature data cannot be absolutely certain. We are confident that the largest temperature oscillations are associated with higher-order eruptions, but a few double eruptions could have been misidentified as single eruptions if their temperature variation and TAE were in the lower range for double eruptions. The number of observed double (11) and triple (3) eruptions is statistically too low to obtain reliable discriminating criteria between double and triple eruptions. In addition, the sensors recorded a minimum and not the actual temperature drop, which implies that the discriminating threshold between double and triple eruptions for the temperature variations is not accurate. In any case, we consider the data set of single eruptions as statistically representative. Our study highlight significant trends for the temperature variations between the different types of eruptions and the recording depths. Future studies could evaluate the true temperature variations during the eruptive cycle with sensors possessing a quasi-instantaneous response time. These studies should also consider a synchronous seismic recording and camera monitoring of the water surface to properly capture the temperature variation with respect to the eruptive cycle and its different phases.

5.3. Heat Transfer and Mass Flow in Strokkur Conduit

Eibl et al. (2021) recognized four distinctive phases in the seismic signal recording an eruptive cycle of Strokkur: (a) eruption, (b) post-eruptive conduit refilling, (c) gas filling of the bubble trap, and (d) bubble collapse. Identifying these four phases in the temperature records is, however, difficult because the water temperature logs reflect different processes (heat transfer and mass flow) and conditions with respect to the seismic oscillations (ground motions associated with wave formation and propagation). We propose a complementary model of conduit dynamics based on the temperature oscillations. Each eruption is followed by a temperature decay and a subsequent temperature increase that we refer to as conduit cooling and conduit warming phases, respectively, to avoid any confusion with the terms "charging" and "discharging" phases that commonly refer to bubble trap processes.

As Eibl et al. (2021) suggest, vapor accumulates at depth within a fixed volume chamber (the "bubble trap") connected with the conduit. The amount of vapor leaving the bubble trap is controlled by the local small temperature and pressure variations in the bubble trap and conduit. The bubble trap modulates gas release based on heat transfer rate (which controls vapor production), its volume (which controls pressure) and the geometry of the neck connecting it to the main conduit (which are associated with periodic emptying and refilling). As bubbles are released from the trap, they rise in the conduit and eventually coalesce into a slug-like structure (Wallis, 1969) leading to a single eruption or, alternatively (if the neck is large enough, as demonstrated by Davidson and Schüler (1960) and Vergniolle and Jaupart (1986)), a slug is directly formed at the bubble trap exit. Our visual evidence from HS imaging at the vent suggests that each eruption is fed by a slug rising in the conduit and generating a series of eruptive bursts. Higher-order eruptions are then associated (Figure 3) to multiple successive releases of vapor from the trap that creates spaced slugs (Vergniolle & Jaupart, 1986), which eventually results in sequences of explosions. This model for slug formation implies similar transient dynamics associated with each cycle/eruption. Each transient is marked by the rise of a mass of vapor through stagnant water filling the conduit. During rise, the slug is expanding according to the hydrostatic pressure gradient. Its drift velocity is proportional via the flow Froude number (Fr) to the square root of gravity and conduit diameter (E. White & Beardmore, 1962). Given that Fr is constant for the condition expected in Strokkur (Wallis, 1969), any slug velocity fluctuation and a final acceleration are only due to irregular conduit geometry and uppermost widening (Figure 3, Walter et al., 2020). However, Fr will be constant among different eruptions, depending only on conduit but not on the volume of the vapor released. For the conditions expected at Strokkur and the conduit diameter, we are expecting a Fr of 0.56 (Viana et al., 2003) and a slug rise velocity of the order of 1 m/s. The rise of the slug in stagnant water will be accompanied by formation of a wake of recirculating water behind it. The dynamics and length of the wake will depend on the balance between viscous and inertial forces as quantified by the dimensionless inverse viscosity number, corresponding to the ratio between the square root of gravity multiplied by the third power of conduit diameter (m^3) and divided by water kinematic viscosity (m^2/s) (Nogueira et al., 2006). Again, for the conditions expected in the conduit at Strokkur, inverse viscosity is much larger than 10^3 and thus water (re-)circulation in the wake will be turbulent. The wake is expected to be up to 10 times longer than the slug (Pinto et al., 1998). Within a single eruption, we associate the first pulse of the water jet with ejection of the water dragged by the slug (the liquid film above the bubble) and successive pulses as due to the wake ejection and eventually to steam flashing in the conduit. The highest exit speeds are reached during wake emission (second pulse). Slug rise will be mostly recorded by pressure fluctuations (Azzopardi et al., 2014), but also by a discontinuity in the temperature rise due to the passage of the wake, which is kept in internal thermal equilibrium by internal liquid (re-)circulation (Shemer et al., 2007; van Hout et al., 2002). The temperature drop during the conduit cooling phase is associated with mass transfer: (a) evacuation of water and vapor associated with the eruption and (b) filling of the conduit by phreatic water through fractures and water cooled in the jet falling back in the vent (Eibl et al., 2021). This results in a more dramatic temperature decay at depth with respect to the shallow conduit, because of the water temperature gradient in the conduit and the more uniform temperature of phreatic water (Lupi et al., 2022). In parallel, duration of the conduit cooling phase decreases with depth. The conduit warming phase has a more complex pattern, being marked by one or more discontinuities in the curve (Figure 3b and Figure S5 in Supporting Information S1) in all records except for S21 (the shallowest). The discontinuity records a short (1–5 s) disturbance (in the form of a plateau), which could be associated with the passage of the vapor mass and its associated (re-)circulation turbulent wake. Unfortunately, the sampling rate and sensor response time were not accurate enough to record the internal dynamics of this structure. These steps in the warming phases could also reflect the heat released by bursting bubbles in the conduit during Phase 4 of the eruptive cycle described by Eibl et al. (2021). Yet, the sampling rate and response time of the sensor do not allow us to conclude on that neither. The general shape and slope of the heating ramps are controlled by heat transfer rates from the deep source (bubble trap?) to the mass of water filling the conduit and are independent from depth. We notice that in higher order eruptions, which are marked by a sequence of two or more water jets, our sensors did record only a "simple" conduit cycle. One possible reason is that the sensors accuracy did not allow for identification of very short warming/cooling phases. Another possible reason is that single jets in a sequence are smaller (i.e., involve smaller masses of water) than single eruptions: the conduit is emptied only partially with no breakup of the warming cycle. However, the TAE increases linearly with the eruption order, consistently with a constant heat supply from depth, Eibl et al. (2020).

5.4. Periodicities of Thermal Oscillations

Strokkur's temperature spectrograms are consistent with the eruptive dynamics. The 4 mHz frequency, coinciding with the average period of the oscillations of S20a, S20b, S22, and S23 (see Table S3 in Supporting Information S1) highlights the overall eruption periodicity, whereas the 1–2 mHz frequency range relates to the occurrence of double or triple eruptions in the same periods (Figures 4 and 5). Temperature oscillations at Great Geysir are not synchronous nor display similar shapes with respect to those recorded at Strokkur. No cross-correlation between Great Geysir and Strokkur temperature signals could be established. A recent geo-electric survey suggested that both geysers would be connected at depth to a same reservoir by a network of fault and fractures (Lupi et al., 2022). However, deep signals are likely modulated by the complex geometry of this connection, hampering any synchronicity in the temperature records. Great Geysir's thermal spectrum is missing the 4 mHz peak, suggesting that the general Strokkur's eruption dynamics (and associated energy releases) do not affect Great Geysir and likely the general system. A frequency peak near 1 mHz is instead observed on the spectrograms of both Great Geysir and Strokkur, although they are shifted in time (Figure 4). This suggests that this frequency component, also associated with higher order eruptions at Strokkur, might be associated with deep seated processes, or alternatively, that larger energy discharges of the Strokkur system could also have an effect on Great Geysir dynamics. The 1 mHz peak frequency in Great Geysir spectrogram do not also relate to the periods of the thermal cycles, identified from peak to peak analyses. This can be due to the automatic selection and the complex nature of the signal at Great Geysir. The threshold value (just above instrument resolution) used for peak selection represent about 20% of the maximum amplitude of the signal, which explains the selection or not of some peaks. This may also explain the discrepancy in the periodicity of the thermal cycles of G22, with respect to G21 and G23. The complex temperature pattern at Great Geysir could also be related to the relatively shallow depth of the measurement, at which surface conditions can affect more the water temperature than deeper processes. Further studies investing a possible connection between both geysers should immerse sensors with a higher temperature resolution at greater depths. Our measurements cannot explain the observed eruption periodicity, which is controlled by source dynamics: steady conditions in the experimental period and also across the previous year (Eibl et al., 2020) do not allow any accurate modeling of the source parameters nor the bubble trap capacity.

6. Conclusions

This study shows for the first time the transient temperature evolution inside the conduits of the active Strokkur and the quasi-dormant Great Geysir geysers in the Haukadalur hydrothermal field, Iceland. The consistency of dynamics and frequency of Strokkur's eruptions allowed us to collect a representative data set and the temperature evolution at different depths inside the conduit during several eruptive cycles. Periodicity of the temperature oscillations are associated with the eruptive dynamics and/or the general system dynamics. At Strokkur we identified eruptive cycles for single, double and triple eruptions from its temperature records and visual observation of the eruptive activity. The TAE for our identified eruptions agrees with previous studies and between the different days of recording, confirming the regularity of Strokkur's eruptions. Based on the temperature records, we analyze the conduit cooling and subsequent warming phases that follow an eruption. After an eruption, the conduit is refilled by both water falling back from the jet in the pond and laterally from the phreatic water. In the meanwhile, new vapor accumulates in the bubble trap. Temperature rise is associated with heat transfer from depth, while temperature drop is due to conduit refill in the few seconds following the eruption from water falling back in the pool and feeding from the phreatic water. The temperature variations during the cooling phase increase with depth or with eruption type, showing faster heat transfer in the deeper part than in the shallow part of the conduit and larger heat release by higher-order eruptions. Eruptions consist in a series of vertical pulses of water and steam, emitted at speeds ranging from 4 to 30 m/s. They are preceded by the rise of the water table in the conduit until a large volume of steam breaks the free water surface and exits, dragging jets of water which partly fall back in the pond and partly fragment into a fine aerosol.

Acknowledgments
We thank the Umhverfisstofnun, the Environment Agency of Iceland for the research permit at the Haukadalur hydrothermal field, and the park rangers for their support. O. Rögnvaldsson and G.N. Petersen are thanked for providing information about weather data. This study was partially funded by the Augustin Lombard Scholarship for S. Mueller, who is also thanked for his support in the field. We are grateful to G. Carrier for her help in the field and A. Mazzini for providing support with hardware. M. Collignon was funded by GENERATE (SNF project PYAPP24_66900, PI Matteo Lupi) and also by a Marie Skłodowska-Curie Individual Fellowship (NERUDA 793662). L. Pioli acknowledges the Fond National Suisse project 200021_162439 and the National Science Foundation Grant NSF PHY-1748958. M. Collignon thanks Ø. Hammer, V. Antunes, and T. Planes for fruitful discussions. L. Pioli is grateful to M. Ichihara for fruitful discussions on sensor technology. The authors thank E. Eibl and an anonymous reviwer for their comments and suggestions.

Data Availability Statement

All raw data and scripts to reproduce the results presented in this paper have been placed in two zenodo repositories. Temperature data and matlab scripts to process them can be found in Collignon (2022), whereas high-speed videos can be found in Pioli (2023).

References

Adelstein, E., Tran, A., Munoz-Saez, C., Shteinberg, A., & Manga, M. (2014). Geyser preplay and eruption in a laboratory model with a bubble trap. *Journal of Volcanology and Geothermal Research*, *285*, 129–135. https://doi.org/10.1016/j.jvolgeores.2014.08.005

Anderson, L., Anderegg, J. W., & Lawler, J. (1978). Model geysers. *American Journal of Science*, *278*(5), 725–738. https://doi.org/10.2475/ajs.278.5.725

Azzopardi, B., Pioli, L., & Abdulkareem, L. (2014). The properties of large bubbles rising in very viscous liquids in vertical columns. *International Journal of Multiphase Flow*, *67*, 160–173. https://doi.org/10.1016/j.ijmultiphaseflow.2014.08.013

Belousov, A., Belousova, M., & Nechayev, A. (2013). Video observations inside conduits of erupting geysers in Kamchatka, Russia, and their geological framework: Implications for the geyser mechanism. *Geology*, *41*(3), 387–390. https://doi.org/10.1130/g33366.1

Bryan, T. (1995). *The geysers of Yellowstone: Boulder, Colorado*. University Press of Colorado.

Bunsen, R. (1847). Physikalische beobachtungen ueber die hauptsaechliche geysir islands. *Poggendorffs Ann. Phys. Chem.*, *72*(9), 159–170. https://doi.org/10.1002/andp.18471480911

Collignon, M. (2022). Temperature data Great Geysir and Strokkur (Iceland) [Dataset]. Zenodo. https://doi.org/10.5281/zenodo.8140601

Cros, E., Roux, P., Vandemeulebrouck, J., & Kedar, S. (2011). Locating hydrothermal acoustic sources at old faithful geyser using matched field processing. *Geophysical Journal International*, *187*(1), 385–393. https://doi.org/10.1111/j.1365-246x.2011.05147.x

Davidson, J., & Schüler, B. (1960). Bubble formation at an orifice in a viscous liquid. *Transactions of the Institution of Chemical Engineers*, *75*, S105–S115. https://doi.org/10.1016/s0263-8762(97)80008-1

Droznin, V., Bakhtiyarov, V., & Levin, V. (1999). Temperature measurements in the Velikan geyser basin (valley of geysers, Kamtchatka). *Volcanol. Seismol.*, *21*, 67–78.

Eibl, E. P., Hainzl, S., Vesely, N., Walter, T., Jousset, P., Hersir, G., & Dahm, T. (2020). Eruption interval monitoring at strokkur geyser, Iceland. *Geophysical Research Letters*, *47*, 1–10. https://doi.org/10.1029/2019gl085266

Eibl, E. P., Jousset, P., Dahm, T., Walter, T. R., Hersir, G. P., & Vesely, N. I. (2019). Seismic experiment at the strokkur geyser, Iceland, allows to derive a catalogue of over 70,000 eruptions [Dataset]. https://doi.org/10.5880/GFZ.2.1.2019.005

Eibl, E. P., Müeller, D., Walter, T., Allahbakhsi, M., Jousset, P., Hersir, G., & Dahm, T. (2021). Eruptive cycle and bubble trap of Strokkur geyser, Iceland. *Journal of Geophysical Research: Solid Earth*, *126*, 1–20. https://doi.org/10.1029/2020JB020769

Hurwitz, S., Clor, L. E., McCleskey, R. B., Nordstrom, D. K., Hunt, A. G., & Evans, W. C. (2016). Dissolved gases in hydrothermal (phreatic) and geyser eruptions at Yellowstone national park, USA. *Geology*, *44*(3), 235–238. https://doi.org/10.1130/g37478.1

Hurwitz, S., & Manga, M. (2017). The fascinating and complex dynamics of geyser eruptions. *Annual Review of Earth and Planetary Sciences*, *45*(1), 31–59. https://doi.org/10.1146/annurev-earth-063016-015605

Hutchinson, R., Westphal, J., & Kieffer, S. W. (1997). In situ observations of old faithful geyser. *Geology*, *25*(10), 875–878. https://doi.org/10.1130/0091-7613(1997)025<0875:isooof>2.3.co;2

Ingebritsen, S., & Rojstaczer, S. (1993). Controls on geyser periodicity. *Science*, *262*(5135), 889–892. https://doi.org/10.1126/science.262.5135.889

Ingebritsen, S., & Rojstaczer, S. (1996). Geyser periodicity and the response of geysers to small strains in the earth. *Journal of Geophysical Research*, *101*(B10), 21891–21907. https://doi.org/10.1029/96jb02285

Jones, B., Renaut, R. W., Torfason, H., & Owen, R. B. (2007). The geological history of Geysir, Iceland: A tephrochronological approach to the dating of sinter. *Journal of the Geological Society*, *164*(6), 1241–1252. https://doi.org/10.1144/0016-76492006-178

Kedar, S., Kanamori, H., & Sturtevant, B. (1998). Bubble collapse as the source of tremor at old faithful geyser. *Journal of Geophysical Research*, *103*(B10), 24283–24299. https://doi.org/10.1029/98jb01824

Kieffer, S. W. (1984). Seismicity at old faithful geyser: An isolated source of geothermal noise and possible analogue of volcanic seismicity. *Journal of Volcanology and Geothermal Research*, *22*(1–2), 59–95. https://doi.org/10.1016/0377-0273(84)90035-0

Kieffer, S. W. (1989). Geologic nozzles. *Reviews of Geophysics*, *27*(1), 3–38. https://doi.org/10.1029/rg027i001p00003

Kiryukhin, A., Rychkova, T., & Dubrovskaya, I. (2012). Formation of the hydrothermal system in geysers valley (Kronotsky nature reserve, Kamchatka) and triggers of the giant landslide. *Applied Geochemistry*, *27*(9), 1753–1766. https://doi.org/10.1016/j.apgeochem.2012.02.011

Lupi, M., Collignon, M., Fischanger, F., Carrier, A., Trippanera, D., & Pioli, L. (2022). Geysers, boiling groundwater and tectonics: The 3d subsurface resistive structure of the Haukadalur hydrothermal field, Iceland. *Journal of Geophysical Research: Solid Earth*, *127*(11), e2022JB024040. https://doi.org/10.1029/2022jb024040

Mackenzie, G. (1811). *Travels in the island of Iceland*. Archibald Constable & Co.

Munoz-Saez, C., Manga, M., Hurwitz, S., Rudolph, M. L., Namiki, A., & Wang, C. (2015). Dynamics within geyser conduits, and sensitivity to environmental perturbations: Insights from a periodic geyser in the El Tatio geyser field, Atacama Desert, Chile. *Journal of Volcanology and Geothermal Research*, *292*, 41–55. https://doi.org/10.1016/j.jvolgeores.2015.01.002

Munoz-Saez, C., Namiki, A., & Manga, M. (2015). Geyser eruption intervals and interactions: Examples from El Tatio, Atacama, Chile. *Journal of Geophysical Research: Solid Earth*, *120*(11), 7490–7507. https://doi.org/10.1002/2015jb012364

Namiki, A., Ueno, Y., Hurwitz, S., Manga, M., Munoz-Saez, C., & Murphy, F. (2016). An experimental study of the role of subsurface plumbing on geothermal discharge. *Geochemistry, Geophysics, Geosystems*, *17*(9), 3691–3716. https://doi.org/10.1002/2016gc006472

Noguchi, K., Aikawa, K., Lloyd, E., Simpson, B., & van der Werff, P. (1983). Measurement of the orifice temperature of the Te Horu geyser in Whakarewarewa, New Zealand. In *4th int. symp. water-rock interact* (pp. 363–366).

Nogueira, S., Riethmuller, M., Campos, J., & Pinto, A. (2006). Flow patterns in the wake of a Taylor bubble rising through vertical columns of stagnant and flowing Newtonian liquids: An experimental study. *Chemical Engineering Science*, *61*(22), 7199–7212. https://doi.org/10.1016/j.ces.2006.08.002

Pálmason, G. (2002). Iceland's Geysir aroused by earthquakes in June 2000. *ThE GOSA Transactions*, *7*, 139–147.

Pasvanoglu, S. (1998). Geochemical study of the Geysir geothermal field in Haukadalur, Iceland. In L. Georgsson (Ed.), *United nations university fellows reports 1998* (pp. 281–318). UN Univ. Geotherm. Train. Program.

Pinto, A., Coelho Pinheiro, M., & Campos, J. (1998). Coalescence of two gas slugs rising in a co-current flowing liquid in vertical tubes. *Chemical Engineering Science*, *53*(16), 2973–2983. https://doi.org/10.1016/s0009-2509(98)00121-3

Pioli, L. (2023). Strokkur geyser, Haukadalur hydrothermal field movies [Dataset]. Zenodo. https://doi.org/10.5281/zenodo.8130930

Rinehart, J. (1969). Thermal and seismic indications of old faithful geyser's inner workings. *Journal of Geophysical Research*, *74*(2), 566–573. https://doi.org/10.1029/jb074i002p00566

Rudolph, M. L., & Sohn, R. A. (2017). A model for internal oscillations in geysers, with application to old faithful (Yellowstone, USA). *Journal of Volcanology and Geothermal Research*, *343*, 17–24. https://doi.org/10.1016/j.jvolgeores.2017.04.023

Rudolph, M. L., Sohn, R. A., & Lev, E. (2018). Fluid oscillations in a laboratory geyser with a bubble trap. *Journal of Volcanology and Geothermal Research*, *368*, 100–110. https://doi.org/10.1016/j.jvolgeores.2018.11.003

Saemundsson, K. (1979). Outline of the geology of Iceland. *Jökull Journal*, *29*(1), 7–28. https://doi.org/10.33799/jokull1979.29.007

Schindelin, J., Arganda-Carreras, I., Frise, E., Kaynig, V., Longair, M., Pietzsch, T., et al. (2012). Fiji: An open-source platform for biological-image analysis. *Nature Methods*, *9*(7), 676–682. https://doi.org/10.1038/nmeth.2019

Shemer, L., Gulitski, A., & Barnea, D. (2007). On the turbulent structure in the wake of Taylor bubbles rising in vertical pipes. *Physics of Fluids*, *19*(3), 035108. https://doi.org/10.1063/1.2711478

Torfason, H. (1985). *The great Geysir*. Geysir Conservation Committee.

Torfason, H. (1999). Geology of the Geysir area in southern Iceland. In *5th international sympsosium on the geochemistry of the earths surface* (pp. 2–5).

Vandemeulebrouck, J., Roux, P., & Cros, E. (2013). The plumbing of old faithful geyser revealed by hydrothermal tremor. *Geophysical Research Letters*, *40*(10), 1989–1993. https://doi.org/10.1002/grl.50422

Vandemeulebrouck, J., Sohn, R. A., Rudolph, M. L., Hurwitz, S., Manga, M., Johnston, M. J., et al. (2014). Eruptions at lone star geyser, Yellowstone national park, USA: 2. Constraints on subsurface dynamics. *Journal of Geophysical Research: Solid Earth*, *119*(12), 8688–8707. https://doi.org/10.1002/2014jb011526

van Hout, R., Gulitski, A., Barnea, D., & Shemer, L. (2002). Experimental investigation of the velocity field induced by a Taylor bubble rising in stagnant water. *International Journal of Multiphase Flow*, *28*(4), 579–596. https://doi.org/10.1016/s0301-9322(01)00082-9

Vergniolle, S., & Jaupart, C. (1986). Separated two-phase flow and basaltic eruptions. *Journal of Geophysical Research*, *91*(B12), 12842–12860. https://doi.org/10.1029/jb091ib12p12842

Viana, F., Pardo, R., Yanez, R., Trallero, J. L., & Joseph, D. D. (2003). Universal correlation for the rise velocity of long gas bubbles in round pipes. *Journal of Fluid Mechanics*, *494*, 379–398. https://doi.org/10.1017/s0022112003006165

Wallis, G. (1969). *One-dimensional two-phase flow*. McGraw-Hill.

Walter, T., Jousset, P., Allahbakhsi, M., Witt, T., Gudmundsson, M. T., & Hersir, G. (2020). Underwater and drone based photogrammetry reveals structural control at Geysir geothermal field in Iceland. *Journal of Volcanology and Geothermal Research*, *391*, 1–9.

White, D. (1967). Some principles of geyser activity, mainly from steambot springs, Nevada. *American Journal of Science*, *265*(8), 641–684. https://doi.org/10.2475/ajs.265.8.641

White, E., & Beardmore, R. (1962). The velocity of rise of single cylindrical air bubbles through liquids contained in vertical tubes. *Chemical Engineering Science*, *17*(5), 351–361. https://doi.org/10.1016/0009-2509(62)80036-0

References From the Supporting Information

Hurwitz, S., Sohn, R. A., Luttrell, K., & Manga, M. (2014). Triggering and modulation of geyser eruptions in Yellowstone national park by earthquakes, earth tides, and weather. *Journal of Geophysical Research: Solid Earth*, *119*(3), 1718–1737. https://doi.org/10.1002/2013jb010803